Third-order momentum advection on the quasi-hexagonal C-grid on the sphere

Almut Gassmann

Alte Molkerei 3, 18225 Kühlungsborn, Germany

Key Points:

- Third-order momentum advection alleviates dispersion errors and avoids spuriously generated gravity waves in atmosphere and ocean models.
- Advection is split into a second-order part and a higher order diffusive/antidiffusive add-on. This allows for energy conservation.
- Trivariate coordinate lines or their appoximations on distorted grids are necessary for the technical realization on the hexagonal C-grid.

Corresponding author: Almut Gassmann, agassman@posteo.de

Abstract

The 3rd-order upstream advection scheme for scalars on the Voronoi C-grid, once introduced by Skamarock and Gassmann (2011), is applied to horizontal momentum advection. A prerequisite is that the 2nd-order momentum advection is available in advection form for a trivariate coordinate system, so that the higher order terms can be formulated as an add-on. Three key ingredients for a successful application are (i) the determination of the advecting velocity, (ii) the determination of directional Laplacians of wind components and (iii) the determination of the upstream direction. The scheme is tested in two settings, a shallow water framework on the regular hexagonal mesh and the baroclinic wave test on the sphere, where the mesh is slightly deformed. In both cases, the trailing ripples and waves known to represent dispersion errors are impressively reduced. If they are not removed, they can lead to spurious excitation of gravity waves or wavy vorticity patterns. After upscale error growth, they can no longer be identified as a result of numerical errors. The effects of the 3rd-order upstream add-on and a Smagorinsky diffusion are compared. The Smagorinsky model reduces the amplitude of the mentioned waves, but does not erase them. With regard to the dissipation properties, the Smagorinsky diffusion is in accordance with the 2nd law of thermodynamics and dissipation is locally only positive. In contrast, dissipation can be locally negative in runs with the 3rd-order upstream add-on. Therefore, physical and numerical requirements cannot be fulfilled simultaneously.

Plain Language Summary

This paper deals with precise calculation methods for the transport of wind. These have been applied to the quadrilateral grid, which is similar to our geographical coordinates. Here, for the first time, we apply them to the hexagonal C-grid which means that the wind variables are given as being perpendicular to the edges of slightly deformed hexagons or pentagons. With such a grid covering the sphere, the areas of these polygons are almost equal, even at the poles. The inaccuracy of the standard calculation method for wind transport is expressed by the generation of 'gravity waves' in the upstream direction of the flow. Because they may travel long distances in the atmosphere, they may alter the flow at distant regions. With the new method, these deceptive waves can be largely avoided. This new calculation method has a term which signifies a global kinetic energy loss, which is converted into heat. However, this heating can be locally negative, which is against the 2nd law of thermodynamics. This paper completes the set of numerical methods on hexagonal C-grids and shows it to be fully equivalent to methods on quadrilateral C-grids, with the advantage of having quasi-uniform grid areas over the globe.

1 Introduction

During the last two decades, numerical modeling of atmosphere and ocean has encountered a development boost. Especially the use of finite volume models which are not prone to the pole problem trap has matured. Such models work on the collocated octahedral grid (Kühnlein et al., 2019) or the collocated geodesic grid (Subich, 2018) or on staggered geodesic C-grids (Skamarock et al., 2012; Dubos et al., 2015; Zängl et al., 2015; Gassmann, 2013; Zhang et al., 2019; Ringler et al., 2013; Korn, 2017; Herzfeld et al., 2020). The advantage of finite volume methods on geodesic grids is the the better compatibility with the physics parameterizations because they allow for cleary defined subgid-scale fluxes. This is also central for exchanges between the Earth System components. Remapping between physics and dynamics grids is thus not needed, and the perception of physics and dynamics becomes seamless. The price to pay for such a finite volume concept is that higher order accuracy for advection processes requires special efforts on geodesic grids. C-staggered models are currently only partially equipped

with higher order advection operators, namely only for scalar variables (Skamarock & Gassmann, 2011; Zängl et al., 2015; Miura & Skamarock, 2013) but not for the wind vector. The need for higher than second order advection methods is urgent, because the well-known detrimental dispersion errors of the group velocity in any geophysical variable (Durran, 2010) may initiate spurious gravity waves. Such gravity waves may then be perceived by the model as physical reality (Gassmann, 2021) and they may travel over long distances into the middle atmosphere, where they are initiating further dynamical feedback. Gravity waves themselves are the best numerically modelled in their behaviour when choosing a C-grid discretization (Randall, 1994).

Currently, C-grid discretizations on geodesic grids are available as triangular and hexagonal C-grid variants. Inspecting the dispersion relation of gravity waves has revealed that the hexagonal C-grid exhibits similar numerical wave propagation properties as the well-understood quadrilateral C-grid (Thuburn, 2008; Gassmann, 2011). In contrast, the triangular C-grid features a spurious artificial checkerboard mode in the divergence which has to be controlled by filtering, which is differently achieved in the ICON atmosphere (Zängl et al., 2015) and ocean (Korn, 2017) models and which contradicts the original intention of choosing a C-grid discretization. The triangular C-grid exhibits another drawback which concerns the degree to which a numerical equivalence between the vector invariant and the momentum advection form may be obtained. This is essential, because the Hollingsworth instability (Hollingsworth et al., 1983) as a non-linear instability of the momentum advection discretisation can be traced back to this numerical non-equivalence. This instability expresses itself as spurious small-scale disturbances in the divergence field and is not at first related to vorticity dynamics. It may severely disturb the ability of a model to reproduce realistic dynamics even in today's quadrilateral models (Soontiens & Allen, 2017). It is impossible to derive an equivalence between the vector-invariant and the advection form for the triangular C-grid. On the side of the hexagonal C-grid, also the vector invariant form has been known first (Thuburn et al., 2009; Ringler et al., 2010) (hereafter TRiSK), but Gassmann (2018) (hereafter G18) demonstrated that the equivalence between the advection form and the vector invariant form can be obtained. This is essential, since we need the advection form for another reason, and this is the main topic of the present contribution: We need it for constructing higher order momentum advection. Higher order advection methods need at least the definition of an upstream direction and a coordinate line on which the corrections to the centered difference approach may be computed. Before this advection form was known, upstream advection was only available on the level of the indirectly available vorticity equation (Ringler et al., 2010; Weller, 2012), not on the level of the horizontal momentum equation itself.

Skamarock and Gassmann (2011) (hereafter SG11) established a 3rd-order flux form advection method for scalars on the Voronoi C-grid. The flux at an edge can be separated into two ingredients, a second order flux and an additional term that ensures higher order accuracy. In case fo the 3rd-order scheme, the latter is formulated using a directional Laplacian which is computed in the upstream cell. The scheme can be formally augmented to fourth order by averaging the directional Laplacians of both sides of the edges. The intention of the present paper is to carry this method over to horizontal momentum advection. Several pitfalls complicate this effort for the Voronoi C-grid. It is unclear, at first glance, what the reference cell is, it is unclear, what the edge-normal advective velocity is, and it is unclear how to compute the directional Laplacians of the velocity components.

The strategy I follow here is to leave the second order momentum advection in the vector invariant form as it is. Thereby I rely on the proof already given in G18 that there exists an approximate equivalence to the second order advective form. A short paragraph below will discuss that the terms which spoil the exact equivalence do not give raise to the danger of the Hollingsworth instability. This allows me then focusing only on the higher order correction flux terms. The divergence of these correction fluxes can be cast

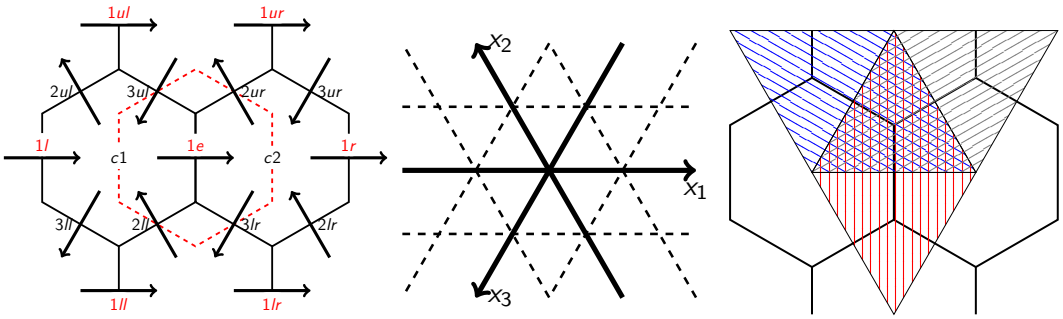

Figure 1. Left: The naming convention for the grid entities used in this paper. The area enclosed by the red dashed lines is the reference area for edge $1e$. The edges are annotated with their coordinate line number {1,2,3} and a marker (ul=upper left, ur=upper right, ll=lower left, lr=lower right) with respect to the edge $1e$. The neighboring cells to edge $1e$ are $c1$ ad $c2$. Middle: The trivariate coordinate system with {1,2,3}-coordinate lines. Right: The rhombi on which the vorticities are defined. With respect to the grid nomenclature on in the left picture, the blue, red and gray hatched rhombi are defined on the edges $3ul$, $1e$ and $2ur$, respectively. Note that they are overlapping.

as a divergence of the stress tensor, but the components of the stress tensor are then not shear and strain deformations, but those higher order flux corrections. Consequently, this tensor violates the 2nd law of thermodynamics, which says that the kinetic energy dissipation into heat must be positive at every point. As discussed in Gassmann (2021), all higher order upstream formulations for scalars share the same property of exhibiting positive and negative local dissipation rates – where clearly the positive dissipation dominates on the global scale. The combination of diffusive and anti-diffusive properties within higher order operators is a side effect of the more well-known goal of higher order schemes, namely the mitigation numerical wave dispersion errors associated with 2nd-order accurate schemes. Thus, formally, numerical aspects and physical aspects are associated with different goals that cannot be brought to match. The reason for this behaviour lies in the very heart of the nature of discretizations on not yet converged scales. Only for DNS scales the viscosity operator is becoming locally so dominant that it offsets the negative effects of numerically introduced anti-diffusive fluxes. The formulation of the upstream add-on in the mathematical structure of a stress tensor allows for the budgeting of the total energy: dissipated (and anti-dissipated) energy is fed back to the internal energy.

The paper is organized as follows. Section 2 describes third order upstream momentum advection for a regular hexagonal C-grid. Section 3 generalizes this method to the slightly deformed mesh case. Section 4 discusses results of test cases for the equilateral shallow water model and for the ICON-IAP model (Gassmann, 2013) run for the baroclinic wave test case. Section 5 concludes the paper.

2 Momentum advection on a regular hexagonal C-grid

2.1 Repetition of the G18 scheme

Figure 1, left, displays the grid entities for a regular equilateral hexagonal C-grid mesh, which are used in this paper. The base vectors pointing into the directions $\{1, 2, 3\}$ establish a trivariate coordinate system (Figure 1, middle panel). The peculiarity of the hexagonal C-grid mesh is that this coordinate system is overspecified. The three base vectors are linearly dependent, and hence the associated measure numbers for the ve-

locity components must remain linear dependent during time stepping, too. If linear dependency is not met, Gassmann (2011, 2018) demonstrated that a checkerboard pattern will appear in the triangle vorticity field. The linear dependency condition poses two constraints on the spatial discretisation procedure for the vector invariant form of the generalized Coriolis term in the linearized limit. First, the TRiSK reconstruction of the tangential wind must be employed. Second, vorticities on distinct positions have to be properly combined with the tangential wind reconstruction (G18). To get an impression how both constraints are combined, consider Figure 1, right. It displays the rhombi on which relevant vorticities for the vorticity flux term are defined. They are all positioned on edges. The energy-conserving G18 scheme means practically that rhombus vorticities ζ_e at 3-positions (e. g. $3ul$, blue) should be combined with 2-position velocity components (e. g. $2ul$ and $2ur$) contributing to tangential wind reconstructions at $1e$ and vice versa.

It is now important to find an at least approximate discrete equivalence between the vector invariant and the advection form. In the continuous case it is easily found for the trivariate coordinate system

$$\mathbf{i}_1 \cdot (-\mathbf{k}\zeta \times \mathbf{v}_h - \nabla_h K_h) \quad = \quad -\frac{2}{3}\left(u_1\partial_1 u_1 + u_2\partial_2 u_1 + u_3\partial_3 u_1\right). \tag{1}$$

Here, u_i are the horizontal wind vector components of $\mathbf{v}_h$ for the specified coordinate lines, K_h is the kinetic energy of the horizontal wind, $\mathbf{k}$ is the vertical unit vector, $\mathbf{i}_1$ is the unit vector in 1-direction, ∇_h is the horizontal gradient operator, and ∂_i are the partial derivatives along the specified coordinate lines.

With the above described generalized Coriolis term and a kinetic energy formulation as in Sadourny (1975) the discrete equivalent of (1) is to be found as (refer to G18, equation (36))

$$\begin{aligned}
&\frac{2\overline{\zeta_3\overline{u_2}^{1}}^{2} + \widehat{\zeta_3 u_2}^{1\perp} - 2\overline{\zeta_2\overline{u_3}^{1}}^{2} - \widehat{\zeta_2 u_3}^{1\perp}}{3\sqrt{3}} - \delta_1\left(\frac{\overline{u_1^2}^{1} + \overline{u_2^2}^{2} + \overline{u_3^2}^{3}}{3}\right) \\
&= -\frac{2}{3}\left(\overline{\overline{u_1}^{1}\delta_1 u_1}^{1} + \overline{\widetilde{u_2}^{1}\delta_2 u_1}^{2} + \overline{\widetilde{u_3}^{1}\delta_3 u_1}^{3}\right) + \frac{d^2}{18}\left(\delta_2(\delta_1 u_2)^2 + \delta_3(\delta_1 u_3)^2\right)
\end{aligned} \tag{2}$$

Here, the overline signifies an ordinary arithmethic mean of two values along a coordinate line, e. g.

$$\overline{u_{1c2}}^{1} = (u_{1e} + u_{1r})/2 \tag{3}$$

the tilde signifies an arithmethic mean of two values where the value which is closer to the target edge $1e$ enters with its double weight, e. g.

$$\widetilde{u_{2u}}^{1} = (u_{2ul} + 2u_{2ur})/3 \tag{4}$$

and the hat marks a special average perpendicular to the 1-direction, e. g.

$$\widehat{\zeta_3 u_2}^{1\perp} = (\zeta_{3lr}u_{2ll} + \zeta_{3ul}u_{2ur})/2 \tag{5}$$

The δ_i-operators are ordinary centered difference derivatives over the dual edge length d, which is the length of one edge of a dual triangle. Later we will also need the primal edge length l, which is the length of one edge of a hexagon, and relates to the dual edge length as $l = d/\sqrt{3}$.

2.2 Discussion of the potential danger of the Hollingsworth instability

It is remarkable that (2) indeed features the requested advection form in the first term on the right. The only difference to the well known discretisation on the comparable quadrilateral C-grid is that the advecting velocities are averaged with the tilde average (4), if the advection is in 2- or 3-direction. The additional second term on the right

of (2) is unexpected and seems to be hardly interpretable in the form in which it is given. In the following, it will be scrutinized with respect to a potential danger of the Hollingsworth instability.

The Hollingsworth instability occurs only in the vector invariant form of the momentum equation, because terms in the vorticity flux term and in the kinetic energy gradient term do not cancel each other. For example on a quadrilateral mesh, $-u\partial_y u + \partial_y u^2/2$ does not cancel out in the numerical realization of the v-equation. Therefore the instability occurs already when the model's task is keeping a zonal flow in balance, hence keeping a zero v. A vertical shear acts then as an amplifier of the instability, as was demonstrated by Gassmann (2013). This severe amplification in a 3-dimensional atmosphere is not present in shallow water flow, and therefore this instability is hard to detect in two-dimensional setups. One has use tiny fluid depths in order to initiate it (Hollingsworth et al., 1983).

When considering the vorticity equation, it is unimportant whether terms between the gradient of the kinetic energy and the generalized Coriolis term cancel out or not: the curl of a gradient vanishes anyway in the continuous equation and also in its C-grid discretisation. But for the horizontal divergence D equation, this cancellation is important. Therefore here we discuss the role, which the additional second terms on the right of (2) play in the divergence equation alone

$$\begin{aligned} \partial_t D|_{add\ terms} &= \frac{d^2}{18}(\delta_1(\delta_2(\delta_1 u_2)^2 + \delta_3(\delta_1 u_3)^2) \\ &\quad \delta_2(\delta_3(\delta_2 u_3)^2 + \delta_1(\delta_2 u_1)^2) \\ &\quad \delta_3(\delta_1(\delta_3 u_1)^2 + \delta_2(\delta_3 u_2)^2)). \end{aligned} \tag{6}$$

This expression is now rearranged by swapping the sequence of derivatives. It gives then

$$\begin{aligned} \partial_t D|_{add\ terms} &= \frac{d^2}{18}(\delta_1(\delta_2(\delta_2 u_1)^2 + \delta_3(\delta_3 u_1)^2) \\ &\quad \delta_2(\delta_1(\delta_1 u_2)^2 + \delta_3(\delta_3 u_2)^2) \\ &\quad \delta_3(\delta_1(\delta_1 u_3)^2 + \delta_2(\delta_2 u_3)^2)). \end{aligned} \tag{7}$$

Under this perspective, it looks like the second term of (2) could actually be replaced with

$$\frac{d^2}{18}\left(\delta_2(\delta_1 u_2)^2 + \delta_3(\delta_1 u_3)^2\right) \Rightarrow \frac{d^2}{18}\left(\delta_2(\delta_2 u_1)^2 + \delta_3(\delta_3 u_1)^2)\right). \tag{8}$$

This is clearly not the case in the momentum equation, but from the perspective of the divergence equation, this replacement could have been occurred in the momentum equation. Hence, here, we see that this expression looks like a diffusion along the coordinate axes 2 and 3 with diffusion coefficients ν proportional to a part of the local shear, e. g. $\nu \to \delta_2 u_1\ d^2/18$ and $\nu \to \delta_3 u_1\ d^2/18$. This is in some sense similar to a diffusion, but the diffusion coefficient is not automatically positive, but might have either sign, and therefore in the mean, these additional terms are not diffusive. We know that the whole scheme is in fact energy conserving.

Generalizing the knowledge from the quadrilateral grid to a general case means that non-cancellations of terms containing velocity components which are not parallel to the prognostic wind component constitute the spoiling effects. When looking at the last group of terms in (2) this seems to be indeed the case. So, in the equation for the 1-component some differences of 2- and 3- components appear. But the reformulation (8) reveals that the differences appear as differences of the same component, hence in the 1-component equation the additional differences are again differences of the 1-component. The reformulation (8) does not mingle errors in one wind component into errors of another one. In conclusion we state that the additional terms in (2) are not problematic with respect to a potential numerical non-cancellation instability as firstly described in Hollingsworth et al. (1983).

2.3 Third order upstream scheme for momentum

The flux formulation for higher order fluxes of scalars ψ of SG11 is repeated here. The scalar flux across an edge reads

$$F(\psi)_e = \varrho_e u_e \left(\frac{\psi_{c1} + \psi_{c2}}{2} - \frac{1}{12}(\delta_x^2 \psi_{c1} + \delta_x^2 \psi_{c2}) + \mathrm{sign}(u_e) \frac{\beta}{12}(\delta_x^2 \psi_{c2} - \delta_x^2 \psi_{c1}) \right) \tag{9}$$

if the edge e normal points from cell $c1$ to cell $c2$. The normal wind component and the density at this edge are u_e and ϱ_e, respectively. The coefficient $\beta = 1$ delivers the third order flux, whereas $\beta = 0$ gives the fourth order flux. The directional Laplacians $\delta_x^2 \psi_c$ are here defined without dividing by the squared grid point distances. The first term in parentheses serves delivering the second order flux, and the rest is the higher-order add-on.

When transferring this viewpoint to the momentum advection, we consider the second order advection to be already treated within the vector invariant context as layed down in section 2.1. Hence, only the terms with the directional Laplacians are to be adjusted for higher order momentum advection as well as the actual advecting velocity. Regarding the latter, we noted that for the 2- and 3-directions transport of the 1-component, the advective velocity is actually the tilde-averaged velocity. At the target edge $1e$ we have the following advective tendency along the 2-direction

$$\partial_t u_{1e} = \ldots - \frac{2}{3} \left(\frac{1}{2} \left(\frac{u_{2ul} + 2u_{2ur}}{3} \frac{u_{1ul} - u_{1e}}{d} + \frac{u_{2lr} + 2u_{2ll}}{3} \frac{u_{1e} - u_{1lr}}{d} \right) \right). \tag{10}$$

An astonishing feature here is that the velocities at the edges $3ul$ and $3lr$ are not the same if seen from the perspectives of the target edges $1e$ and $1ul$, respectively. Seen from the perspective of the target edge $1e$, the edge normal velocity at edge $3ul$ is $(u_{2ul}+2u_{2ur})/3$. However, the perspective of the target edge $1ul$ delivers the edge normal velocity to be $(2u_{2ul}+u_{2ur})/3$. When focusing on a flux form formulation of the higher order correction terms of advection, the fluxes must be continuous at the edges of a reference cell. We follow here a strategy that takes the average of both perspectives for the higher order correction fluxes. This is then just half the sum of u_{2ul} and u_{2ur}.

Practically, the higher order flux correction can be cast in a form which is similar to the divergence of a momentum diffusion tensor. G18 has given such a general momentum diffusion formulation for the hexagonal mesh, which reads in the trivariate coordinate system

$$\begin{pmatrix} \partial_t u_1 \\ \partial_t u_2 \\ \partial_t u_3 \end{pmatrix} = -\frac{1}{\varrho} (\partial_1, \partial_2, \partial_3) \cdot \begin{pmatrix} G^{11-23} & G^{12} & G^{31} \\ G^{12} & G^{22-31} & G^{23} \\ G^{31} & G^{23} & G^{33-12} \end{pmatrix} \tag{11}$$

where the G^{ij} and G^{ii-jk} are negative shear and strain deformations multiplied with some dynamic viscosity[1]. The tensor used therein exhibits the usual properties of symmetry and invariance to solid body rotation usually put as physical constraints. Seen from the side of a numerical discretisation, such a symmetric positive definite tensor approach is only meaningful for the case when numerical dispersion errors would be negligible and a physical reality can be imposed for the dissipation scale. Since dispersion errors of the shortest resolvable waves are appearing in the upstream direction (Durran, 2010), we have to use a tensor which deviates from the pure physical principles and takes this upstream direction into account. We have to acknowledge the fact that numerical errors and physical principles are interfering here in inextricable contradiction. Nevertheless, the tensor formulation is very helpful in the sense that the dissipated kinetic energy which is

[1] The exact shapes of the deformations are given in G18, but are irrelevant for the current argumentation line.

finally converted into heat can be retrieved easily also in the discretised case. It gives

$$\begin{aligned}\varepsilon &= -G^{11-23}\partial_1 u_1 - G^{22-31}\partial_2 u_2 - G^{33-12}\partial_3 u_3 \\ &\quad -G^{12}(\partial_1 u_2 + \partial_2 u_1) - G^{31}(\partial_3 u_1 + \partial_1 u_3) - G^{23}(\partial_2 u_3 + \partial_3 u_2) \end{aligned} \tag{12}$$

Clearly, for a positive-definite symmetric tensor, this gives a positive number and is thus in accordance with the second law of thermodynamics in every point. In a strict physical sense, this energy is not directly converted into heat, but it is the shear production that enters the TKE-equation. Only after processed within the TKE-equation, the respective energy is dissipated in the molecular sense. As we shall see, the posititivity of dissipation will only be met in the mean for the upstream add-on, but not pointwise.[2]

Now, let us return to (9) and cast the higher order correction terms in the previously described tensor form. The non-dimensional directional Laplacian along a coordinate line is easy to obtain: It reads for the j-velocity components $\delta_i^2 u_j = u_{ji+1} - 2u_{ji} + u_{ji-1}$ where the indices i are counted along the coordinate line direction i. For the equation at the target edge $1e$ this reads

$$\begin{aligned}\partial_t u_{1e} &= \cdots - \frac{1}{\bar{\varrho}^1|_{1e}}\frac{2}{3}\frac{1}{d}\Big(\\ &\quad +\overline{\varrho u_1}^1|_{c2}\Big(-\frac{1}{12}(\delta_1^2 u_1|_{1r} + \delta_1^2 u_1|_{1e}) + \mathrm{sign}(\overline{u_1}^1|_{c2})\frac{\beta}{12}(\delta_1^2 u_1|_{1r} - \delta_1^2 u_1|_{1e})\Big) \\ &\quad -\overline{\varrho u_1}^1|_{c1}\Big(-\frac{1}{12}(\delta_1^2 u_1|_{1e} + \delta_1^2 u_1|_{1l}) + \mathrm{sign}(\overline{u_1}^1|_{c1})\frac{\beta}{12}(\delta_1^2 u_1|_{1e} - \delta_1^2 u_1|_{1l})\Big) \\ &\quad +\overline{\varrho u_2}^1|_{3ul}\Big(-\frac{1}{12}(\delta_2^2 u_1|_{1ul} + \delta_2^2 u_1|_{1e}) + \mathrm{sign}(\overline{u_2}^1|_{3ul})\frac{\beta}{12}(\delta_2^2 u_1|_{1ul} - \delta_2^2 u_1|_{1e})\Big) \\ &\quad -\overline{\varrho u_2}^1|_{3lr}\Big(-\frac{1}{12}(\delta_2^2 u_1|_{1e} + \delta_2^2 u_1|_{1lr}) + \mathrm{sign}(\overline{u_2}^1|_{3lr})\frac{\beta}{12}(\delta_2^2 u_1|_{1e} - \delta_2^2 u_1|_{1lr})\Big) \\ &\quad +\overline{\varrho u_3}^1|_{2ll}\Big(-\frac{1}{12}(\delta_3^2 u_1|_{1ll} + \delta_3^2 u_1|_{1e}) + \mathrm{sign}(\overline{u_3}^1|_{2ll})\frac{\beta}{12}(\delta_3^2 u_1|_{1ll} - \delta_3^2 u_1|_{1e})\Big) \\ &\quad -\overline{\varrho u_3}^1|_{2ur}\Big(-\frac{1}{12}(\delta_3^2 u_1|_{1e} + \delta_3^2 u_1|_{1ur}) + \mathrm{sign}(\overline{u_3}^1|_{2ur})\frac{\beta}{12}(\delta_3^2 u_1|_{1e} - \delta_3^2 u_1|_{1ur})\Big) \\ &\quad \Big) \end{aligned} \tag{13}$$

Later, on a deformed mesh, the direct differences along the 2 and 3 directions are not available. To eliminate this difficulty, the higher order correction in the 2 and 3 directions are reformulated using a derivative perpendicular to the 1-direction which is taken along a primal edge length l

$$\begin{aligned}\partial_t u_{1e} &= \cdots - \frac{1}{\bar{\varrho}^1|_{1e}}\frac{1}{d}\Big(\\ &\quad +\frac{2\overline{\varrho u_1}^1|_{c2}}{3}\Big(-\frac{1}{12}(\delta_1^2 u_1|_{1r} + \delta_1^2 u_1|_{1e}) + \mathrm{sign}(\overline{u_1}^1|_{c2})\frac{\beta}{12}(\delta_1^2 u_1|_{1r} - \delta_1^2 u_1|_{1e})\Big) \\ &\quad -\frac{2\overline{\varrho u_1}^1|_{c1}}{3}\Big(-\frac{1}{12}(\delta_1^2 u_1|_{1e} + \delta_1^2 u_1|_{1l}) + \mathrm{sign}(\overline{u_1}^1|_{c1})\frac{\beta}{12}(\delta_1^2 u_1|_{1e} - \delta_1^2 u_1|_{1l})\Big)\Big) \\ &\quad -\frac{1}{\bar{\varrho}^1|_{1e}}\frac{1}{3l}\Big(\\ &\quad +\frac{2\overline{\varrho u_2}^1|_{3ul}}{\sqrt{3}}\Big(-\frac{1}{12}(\delta_2^2 u_1|_{1ul} + \delta_2^2 u_1|_{1e}) + \mathrm{sign}(\overline{u_2}^1|_{3ul})\frac{\beta}{12}(\delta_2^2 u_1|_{1ul} - \delta_2^2 u_1|_{1e})\Big) \end{aligned}$$

[2] The terminus dissipation is so overloaded with different meanings in the literature, that a clear definition is necessary in the present context. Dissipation is here meant in its thermodynamic sense. It is an irreversible energy loss of kinetic energy which must be fed into the internal energy through energy conversion. In traditional numerical literature, the terminus dissipation is invoked to the lowest-order even derivative in the modified equation (Durran (2010), Chapter 3.3.2). The dissipation scale in a kinetic energy spectrum is another hint on dissipation, can however not directly be translated in a local feature.

$$
\begin{aligned}
&-\frac{2\overline{\varrho u_2}^1|_{3lr}}{\sqrt{3}}\left(-\frac{1}{12}(\delta_2^2 u_1|_{1e}+\delta_2^2 u_1|_{1lr})+\mathrm{sign}(\overline{u_2}^1|_{3lr})\frac{\beta}{12}(\delta_2^2 u_1|_{1e}-\delta_2^2 u_1|_{1lr})\right)\\
&+\frac{2\overline{\varrho u_3}^1|_{2ll}}{\sqrt{3}}\left(-\frac{1}{12}(\delta_3^2 u_1|_{1ll}+\delta_3^2 u_1|_{1e})+\mathrm{sign}(\overline{u_3}^1|_{2ll})\frac{\beta}{12}(\delta_3^2 u_1|_{1ll}-\delta_2^2 u_1|_{1e})\right)\\
&-\frac{2\overline{\varrho u_3}^1|_{2ur}}{\sqrt{3}}\left(-\frac{1}{12}(\delta_3^2 u_1|_{1e}+\delta_3^2 u_1|_{1ur})+\mathrm{sign}(\overline{u_3}^1|_{2ur})\frac{\beta}{12}(\delta_3^2 u_1|_{1e}-\delta_3^2 u_1|_{1ur})\right)\\
&) \qquad (14)
\end{aligned}
$$

This form is inspired by the form in which we would write down a vector invariant form of the momentum diffusion (see G18), namely

$$\Delta u = \partial_x D - \partial_x^{\perp}\zeta^a = \partial_x D - \partial_x^{\perp}\frac{\zeta_1+\zeta_2+\zeta_3}{3} \qquad (15)$$

where the averaged vorticity over three vorticities on rhombi, which is stored at vertices (triangle midpoints), is actually relevant. This differs from the usual perception of a relevant vorticity measure as defined on triangles. In the numerical realization of the second term on the target edge $1e$, the differences between the ζ_1 values would be zero, because the same vorticity is once added and once removed, the actual differences of the ζ_3 (ζ_2) values would be between the upper left (right) value and the lower right (left) values. The latter feature establishes in fact a difference along the 2 (negative 3) coordinate line. Hence, this didactic detour leads to the conclusion that the directional Laplacians in (14) have to be attached to cells in case of the derivatives along the 1-direction and to rhombi in case of the derivatives along the 2- and 3- directions.

3 Deformed mesh case

3.1 Preliminaries

The coordinate lines are no longer present in the case of a deformed mesh as we encounter it on the sphere. This has the consequences that the following entities which appear in (14) have to be determined on a deformed mesh:

1. the advective velocities
2. the non-dimensional directional Laplacians
3. the upstream located non-dimensional directional Laplacians

The related steps are explained in the following subsections.

Before turning our attention to the upstream add-on terms, a modification of the energy conserving 2nd-order scheme of G18 is shortly discussed here. Namely, if there is a significant weight of an edge e' which is two edges apart from the target edge $1e$ in the TRiSK vector reconstruction, G18 proposed to use the average of the edge vorticities of the respective edges, namely $1e$ and e'. Experience suggests that even better results can be obtained when instead taking the average of the four rhombus vorticities on the respective hexagon edges, which are *neither* the target edge $1e$ *nor* the touched edge e', hence

$$\zeta_{1e,e'}|_{2\ edges\ apart} = \frac{1}{4}\sum_{e''\in c, e''\notin\{e,e'\}}\zeta_{e''} \qquad (16)$$

Namely then, the vorticities entering the generalized Coriolis term are more similar to those entering the other edges. For instance, considering Figure 1 and assuming the reconstruction weight at edge $1l$ was non-zero, the entering vorticities at $3ul$ and $2ll$ are already contributing in other terms, and only the vorticities at $2ul$ and $3ll$ appear additionally because of the deformed mesh.

3.2 Determination of the advective mass fluxes

The relevant advecting mass flux in the 2- and 3- directions in (14) is, for instance at the position $3ul$,

$$\frac{2\overline{\bar{\varrho}^2 u_2}^1|_{3ul}}{\sqrt{3}}. \tag{17}$$

When the weights $w_{e,e'}$ of the TRiSK vector reconstruction are available from Thuburn et al. (2009), they can be exploited in order to give a consistent reconstruction. Since we need a continuous flux over the edge, contributions of the TRiSK vector reconstructions as seen from target edges $1e$ and $1ul$ enter this formulation. Considering that the weights which are two edges away from the target edge contribute with a weight of each one half to the weight-adjusted advective velocity to the upper or lower part of the hexagon, respectively, a deformed mesh realization gives

$$\begin{aligned}\frac{2\overline{\bar{\varrho}^2 u_2}^1|_{3ul}}{\sqrt{3}} &:= 2(w_{1e,2ur}\bar{\varrho}^2 u_{2ur} + w_{1e,2ul}\bar{\varrho}^2 u_{2ul} + \frac{1}{2}w_{1e,1l}\bar{\varrho}^1 u_{1l} \\ &\quad + w_{1ul,2ur}\bar{\varrho}^2 u_{2ur} + w_{1ul,2ul}\bar{\varrho}^2 u_{2ul} + \frac{1}{2}w_{1ul,1r}\bar{\varrho}^1 u_{1r})\end{aligned} \tag{18}$$

A least squares vector reconstruction as laid out in the appendix is used for the vector reconstruction in the centers of the hexagons in the coordinate system of the target edge $1e$, hence

$$\varrho u_{1e,c} := \frac{2}{3}\sum_{e'\in c} r_{1e,e'}\bar{\varrho}^{e'} u_{e'} \tag{19}$$

where the reconstruction weights are $r_{1e.e'}$.

3.3 Determination of the non-dimensional directional Laplacians

G18 explained how a momentum diffusion tensor with local strain and shear deformations may be formulated on the deformed mesh. The generating formula for the Smagorinsky (1993) momentum diffusion adapted for the C-grid Voronoi meshes was

$$\partial_t u_{1e}|_{mom\ diff} = \frac{1}{\varrho}\left(\delta_1^{dim}(\varrho K_c E^1) + \frac{1}{3}\delta_1^{\perp,dim}(\varrho K_2 F_2^1 + \varrho K_3 F_3^1)\right) \tag{20}$$

where the superscript *dim* is a reminder that in this formulation the gradients have dimensions in contrast to the non-dimensional Laplacian which we need later. The $\perp$-operator signifies a finite difference perpendicular to the local edge normal. This corresponds to the already given formulation (14). The shear F_2^1, F_3^1 deformations are located at centers of 2- and 3-rhombi. In Figure 1, a typical 2-rhombus is hatched in gray and the 3-rhombus is hatched in blue. Strain deformations E^1 are located at cell centers. Both types of deformations have to be obtained by reconstructions. Parts of this scheme are reused here for the determination of the directional gradients. The appendix collects the relevant reconstructions. Having the directional wind gradients at hand, directional Laplacians are easy to be obtained. The diffusion coefficients K_c, K_2, K_3 and the densities are then irrelevant and therefore omitted.

The non-dimensional directional Laplacians are determined via a 3-step method:

1. Determination of directional wind gradients.
   The directional wind gradients which point into the same direction as the subsequent differentiation are reconstructed with the least squares method. Thus,

$$E^1 = \frac{2}{3}\delta_x^{dim} u|_c \tag{21}$$

$$F_2^1 = \delta_y^{dim} u|_2 \tag{22}$$

$$F_3^1 = \delta_y^{dim} u|_3 \tag{23}$$

are the reconstructed directional gradients in a (x, y)-coordinate which is confined to the local target edge $1e$, u is then the $1e$-edge-normal wind component. Note that we have to scale the three directional Laplacians correctly, so that in the equilateral limit each directional Laplacian occurs with the weight of 2/3. Therefore, (21) is multiplied by 2/3, but (22) and (23) are not multiplied because the finite difference in the equilateral limit is implicitly taken over the height of a triangle $h = \sqrt{3}d/2$, the subsequent finite difference is over the primal edge length $l = d/\sqrt{3}$, and the final division is by 3.

2. Determination of the directional Laplacians on each edge.
From the given directional gradients directional Laplacians are formed. They are stored independently on each target edge. Hence

$$\delta_{11}^{dim} u_{1e} = \delta_1^{dim} E^1 \tag{24}$$
$$\delta_{22}^{dim} u_{1e} = \delta_1^{\perp,dim} F_3^1 \tag{25}$$
$$\delta_{33}^{dim} u_{1e} = \delta_1^{\perp,dim} F_2^1 \; (= -\delta_1^{\perp,dim}(-F_2^{1*})) \tag{26}$$

The expression in braces highlights that the 3-direction and so the y-derivative in a more stringent version of F_2^{1*}, where the differentiation is already in the negative y-direction, are indeed pointing in the negative perpendicular direction.

3. Non-dimensionalisation of the directional Laplacians.
In order to obtain the required non-dimensional Laplacians in the same form as it was the case in the scalar advection scheme of SG11, a non-dimensionalisation of the directional Laplacians is performed

$$\delta_{ii} u_{1e} = \delta_{ii}^{non-dim} u_{1e} = \frac{3}{2} d_{1e}^2 \delta_{ii}^{dim} u_{1e} \tag{27}$$

where d_{1e}^2 is the squared grid distance between the adjacent cells at point $1e$. Each edge stores now three local non-dimensional directional Laplacians $\delta_{11} u_{1e}$, $\delta_{22} u_{1e}$ and $\delta_{33} u_{1e}$.

3.4 Determination of the upstream value of the non-dimensional directional Laplacians

The most intricate part of the upstream advection formulation is the determination of the upstream direction. Before proceeding we repeat the procedure of SG11 as it is there given for scalars ψ. We do this for didactic reasons, and write once again

$$F(\psi)_e|_{uc} = -\varrho u_e \frac{1}{12} \left((\delta_{xx}\psi|_{c1} + \delta_{xx}\psi|_{c2}) - \mathrm{sign}(u_e)\beta(\delta_{xx}\psi|_{c2} - \delta_{xx}\psi|_{c1}) \right) \tag{28}$$

as an expression for the upstream correction uc-flux. We observe that the second group of terms is a non-dimensional directional gradient of the directional Laplacians, whereas the first term is just twice their mean. When adapting the scheme to the deformed mesh and for momentum components, we find that the velocities appear as reconstructed at the edges of the red reference area of Figure 1, which are at the same time the centers of cells and rhombi. The directional Laplacians obtained in the previous step are located at the edges of these hexagons and rhombi.

Considering the last term of (28), it is clear that the directional gradient of the directional Laplacians has to be obtained in some way at the centers of hexagons and rhombi. Two problems arise with this attempt. First, we cannot reuse the directional gradient weights from the previous subsection, but have to determine new weights, because two additional directional projections have to be taken in account. How this is achieved on hexagons and rhombi is explained in the appendix. Second, if we have the directional gradient of the directional Laplacians, we need to non-dimensionalise it. But it is unclear which grid distance is to be multiplied then. Another problem is that least square reconstructing twice the mean value of the directional Laplacian from the edges of hexagons

or rhombi as needed in the first term in (28) does not deliver a simple mean value of two opposite edges at one coordinate line in case of a regular mesh. Rather, also other edges contribute to the mean in a standard least squares reconstruction.

In order to circumvent the described problems, the following argumentation is pursued. The situation is exemplified for the requested term in x-direction at the $1e$ edge. Then the gradient of the directional Laplacians along local 11-directions[3] at edges e' of the respective cells is located in the cell centers, and it is obtained with predetermined weights $g_{1e,11e'}$. The first index of $g_{1e,11e'}$ refers to the edge generating the coordinate system in which the weights are computed and the second index specifies the involved edges for reconstructions e' as well as the double index of the local directional Laplacians. Here, in the case of the 11-Laplacians, we have

$$\delta_x^{dim}(\delta_{xx}u)|_c = g_{1e,11e}\delta_{1e1e}u_{1e} + \sum_{1e'\in c,1e'\notin 1e} g_{1e,11e'}\delta_{1e',1e'}u_{1e'} \tag{29}$$

The non-dimensionalisation step is invoked by enforcing that the weight at the target edge gives 1, hence

$$\delta_x^{non-dim}(\delta_{xx}u)|_c = \frac{\delta_x^{dim}(\delta_{xx}u)|_c}{g_{1e,11e}} = \delta_{1e1e}u_{1e} + \sum_{1e'\in c,1e'\notin 1e} \frac{g_{1e,11e'}}{g_{1e,11e}}\delta_{1e',1e'}u_{1e'} \tag{30}$$

For the double mean value term we assume that we have a still unknown reconstruction weights $m_{1e,11e'}$, hence

$$2\overline{(\delta_{xx}u)}^{x}|_c = \delta_{1e1e}u_{1e} + \sum_{1e'\in c,1e'\notin 1e} m_{1e,11e'}\delta_{1e',1e'}u_{e'} \tag{31}$$

Combined we can thus write

$$F(u_{1e,c})|_{uc} = -\varrho u_{1e,c}\frac{1}{12}\left(2\overline{(\delta_{xx}u)}^{x}|_c - \beta\mathrm{sign}(u_{1e,c})\gamma_c^{out,1e}\delta_x^{non-dim}(\delta_{xx}u)|_c\right) \tag{32}$$

where $\gamma_c^{out,1e} = \pm 1$ signifies the positive outward (negative inward) direction with respect to the cell c at edge $1e$. In order to determine the $m_{1e,11e'}$-weights, we enforce that if $u_{1e,c}$ is positive and $\beta = 1$, the directional Laplacian at edge $1e$ should be recovered for the flux on the right cell center $c2$, so that in this case

$$F(u_{1e,c2} > 0)|_{uc}^{\beta=1} = -\varrho u_{1e,c2}\frac{1}{12}\left(2\delta_{1e1e}u_{1e}\right). \tag{33}$$

Likewise, the flux on the left cell center $c1$ for a negative velocity should then be

$$F(u_{1e,c1} < 0)|_{uc}^{\beta=1} = -\varrho u_{1e,c1}\frac{1}{12}\left(2\delta_{1e1e}u_{1e}\right). \tag{34}$$

Both of these limit cases deliver for the still undetermined coefficients

$$m_{1e,11e'} = -\frac{g_{1e,11e'}}{g_{1e,11e}}. \tag{35}$$

In fact, this method gives the correct weights when applied for a regular mesh. Finally, the rule (32) can be reformulated in a more compact form

$$F(u_{1e,c})|_{uc} = -\frac{\varrho u_{1e,c}}{12}(2\delta_{1e1e}u_{1e} - (1+\beta\mathrm{sign}(u_{1e,c})\gamma_c^{out,1e})\sum_{1e'\in c,1e'\notin 1e}\frac{g_{1e,11e'}}{g_{1e,11e}}\delta_{1e',1e'}u_{1e'}). \tag{36}$$

[3] For instance for edge $2ur$ the local 11-direction is in fact the (-2)(-2)-direction if seen in the coordinate system of the edge 1e. But since all local directional Laplacians from gradients of the strain deformations E are stored with 11-indices, the code touches only local 11-indexed entities.

A similar reconstruction procedure as described here can be applied to rhombi, and therefore similar upstream flux corrections can be formulated for all three directions. Then, the weights $g_{1e,22e'}$ and $g_{1e,33e'}$ have to be precomputed on rhombi. The appendix describes how the requested gradients of the directional Laplacians in 2- and 3- directions are actually obtained.

Inserting the fluxes obtained in this way into deformed mesh equivalent of (14) delivers the required upstream add-on terms to momentum advection. They are written as

$$\begin{aligned}\partial_t u_{1e} &= \cdots - \frac{1}{\bar{\varrho}^1|_{1e}}\frac{1}{d}\left(F(u_{1e,c2})|_{uc} - F(u_{1e,c1})|_{uc}\right) \\ &\quad -\frac{1}{\bar{\varrho}^1|_{1e}}\frac{1}{3l}\left(\, F(u_{1e,3ul})|_{uc} - F(u_{1e,3lr})|_{uc}\right. \\ &\quad \left. +F(u_{1e,2ll})|_{uc} - F(u_{1e,2ur})|_{uc}\right). \end{aligned} \tag{37}$$

As discussed in (12) for the equilateral grid scheme, we can formulate the kinetic energy dissipation which has to be added as a heating to the internal energy equation. Here, we can make use of the weights $\sigma^D_{e(c)} = l_e\gamma^{out}_{e(c)}/A_c$ and $\sigma^\zeta_{e(r)} = d_e\gamma^{cyclonal}_{e(r)}/A_r$ which are stored as the weights for divergence computation on cells and vorticity computation on rhombi. The computation of the dissipation consists of several steps. First, the dissipation due to the contributions of the fluxes situated on cell centers is obtained via

$$\varepsilon_c = -\sum_{e\in c} u_e(\max(\sigma^D_{e(c)},0)F(u_{e,c1})|_{uc} + \min(\sigma^D_{e(c)},0)F(u_{e,c2})|_{uc}. \tag{38}$$

Second, a similar procedure is performed for the rhombi

$$\begin{aligned}\varepsilon_{r,1e} &= u_{3ul}(\max(\sigma^\zeta_{3ul},0)F(u_{3ul,2ur})|_{uc} + \min(\sigma^\zeta_{3ul},0)F(u_{3ul,2ll})|_{uc}) \\ &\quad u_{2ll}(\max(\sigma^\zeta_{2ll},0)F(u_{2ll,3ul})|_{uc} + \min(\sigma^\zeta_{2ll},0)F(u_{2ll,3lr})|_{uc}) \\ &\quad u_{2ur}(\max(\sigma^\zeta_{2ur},0)F(u_{2ur,3ul})|_{uc} + \min(\sigma^\zeta_{2ur},0)F(u_{2ur,3lr})|_{uc}) \\ &\quad u_{3lr}(\max(\sigma^\zeta_{3lr},0)F(u_{3lr,2ur})|_{uc} + \min(\sigma^\zeta_{3lr},0)F(u_{3lr,2ll})|_{uc}) \end{aligned} \tag{39}$$

The results on rhombi are averaged from edges to cells with weighting factors $A_r/(6A_c)$. Note that in the upstream corrected fluxes, the first index is the one referring tho the actual edge relative to $1e$ and the second index must be understood as the *relative* index with respect to this actual edge, hence it should not be read off from Figure 1. Only in the steps which lead to the momentum diffusion formulation, this actual index was always $1e$ and the *relative* indices could be read off from Figure 1.

4 Results

4.1 SW equilateral mesh case

Before experimenting with the the full atmosphere on the globe where mesh deformation is present, the character of the proposed scheme is studied for a shallow water model on the equilateral mesh. This problem is the simplest setup that we can specify. In contrast to the quasi-linear scalar advection discussed by SG11, the momentum advection is by definition a non-linear process. Therefore standard advection tests with ideal predefined advective velocities are not really applicable. Rather, the following issues are worth to be discussed in the case of nonlinear momentum advection:

- What are the modeled flow differences between the model run with the Smagorinsky diffusion and the upstream add-on?
- Does one need any special measures to suppress the checkerboard mode in the vorticities on triangles?

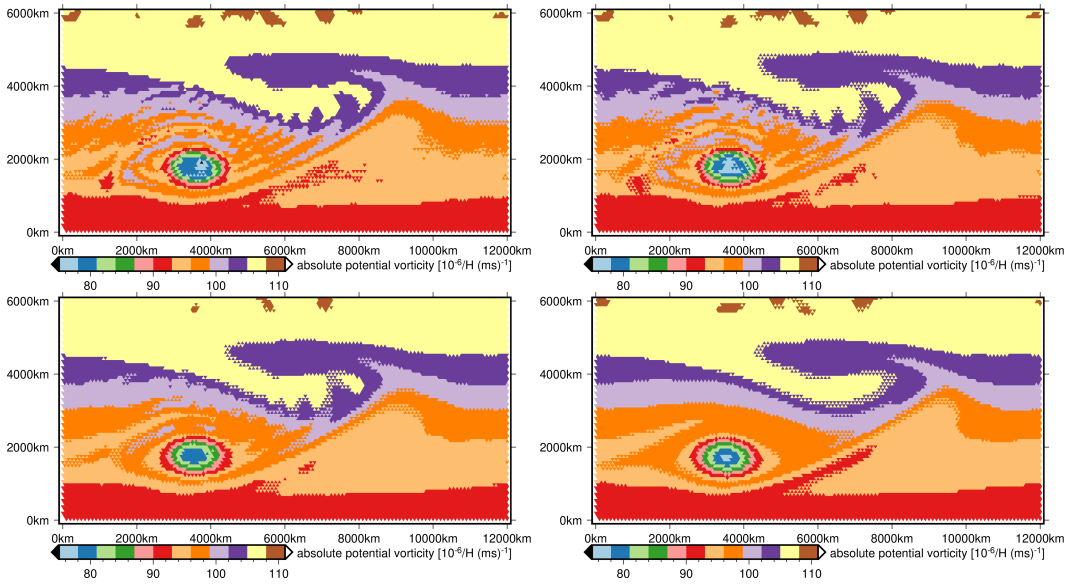

Figure 2. Absolute potential vorticity plotted on triangles for the 5000m depth flow. From top left to bottom right: TRiSK energy conserving scheme, G18 scheme, G18 scheme with Smagorinsky diffusion, G18 with 3rd order upstream add-on.

- Can we learn more about the danger of the Hollingsworth instability by inspecting SW dynamics?

A shallow water model on an equilateral mesh with the dual mesh length of 100 km is set up in a double periodic channel with 12000 km width and 6000 km length. The bottom topography follows a negative cosine profile in the y-direction, so that when choosing a constant fluid thickness a westerly flow is established in the southern half of the domain. Setting the bottom profile to -300 m at the southermost gridline gives about 15 m/s maximal flow speed. Two experiments are now set up with this configuration, one for a fluid thickness of 5000 m and one for a fluid thickness of 0.1 m. The first experiment is designed such as to trigger a significant vortex formation, whereas the second experiment is intended to study the potential danger of the Hollingsworth instability, which is known to appear for small depths. In order to trigger a vortical flow, the fluid depth is perturbed with a 1000 km radius circular shaped thickness surplus of 0.3 times the fluid depth maximum amplitude. The model is then run for 20 days with a timestep of 300 s and RK3 timestepping. Four different configurations for momentum advection and generalised Coriolis term treatment are implemented in the shallow water model: The TRiSK energy conserving scheme, the G18 energy conserving scheme without and with Smagorinsky diffusion, and with the newly proposed 3rd-order upstream add-on.

The results of the 5000 m setup are first discussed. Figure 2 displays the absolute potential vorticity on triangles for all configurations. Note that the vorticity on triangles does not enter in this pure form anywhere in the prognostic equations. But as it is often discussed in the literature (Klemp, 2017; Weller, 2012) that the checkerboard pattern in the vorticity could be problematic, these plots are shown here. Clearly, because the vortex flow is strongly non-linear, one cannot expect that the checkerboard pattern is absent. As already mentioned, the proof of linear dependency of velocity components can only be established in the linear limit. As is seen from Figure 2, all schemes exhibit the checkerboard pattern. Out of the four runs, the G18 run without diffusion features

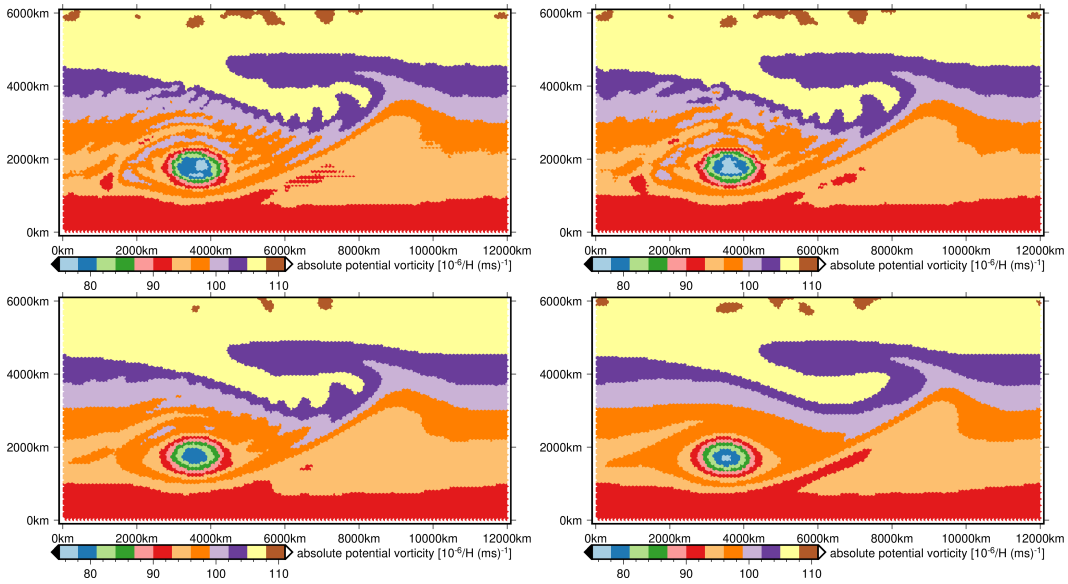

Figure 3. Absolute potential vorticity plotted on edges for the 5000m depth flow. From top left to bottom right: TRiSK energy conserving scheme, G18 scheme, G18 scheme with Smagorinsky diffusion, G18 with 3rd order upstream add-on.

more checkerboard pattern than the TRiSK energy conserving scheme. However, prognostic equations make always use of the vorticities assigned to edges. Hence, when qualitatively judging the potential danger of checkerboard pattern one has to inspect the absolute potential vorticities on edges. They are displayed in Figure 3. Then, only the TRiSK energy conserving scheme shows some small traces of grid scale noise. From these figures, it is clear that no detrimental small scale noise arises on the level of edges for all of the schemes. Therefore the checkerboard on triangles can be ignored and there is no need to defeat these pattern separately as has been suggested by Klemp (2017).

Much more important than the checkerboard noise on triangles is the formation of trailing shortwave perturbations due to well known dispersion errors of centered difference schemes. All configurations besides the 3rd-order upstream momentum advection indeed feature related problems. The TRiSK and the G18 schemes exhibit typical length scales for such ripples starting from $2\Delta x$ up to to much larger wavy pattern. This spread of scales is due to the nonlinear history of the flow field. That means that after a while, larger scale wavy pattern can no longer be attributed by eye interpretation as having their origin in a numerical artefact. They start to become a part of what is generally interpreted a physical reality. The Smagorinsky diffusion can mitigate the amplitude of these ripples and waves, but cannot erase them. Here, a dilemma becomes obvious, Smagorinsky diffusion is always established and discussed as a physically meaningful measure, but it is almost powerless against numerical artefacts, because it does not explicitly fight the origin of those pattern. In contrast and as expected, the 3rd-order scheme is almost free of these ripples, the frontal zone which is stretching from southwest to northeast is more sharply represented and the minimal PV in the center of the cyclone is not eroded.

The small depth experiment is designed to check whether some of the schemes suffer from the Hollingsworth instability. As already explained, this is a feature first appearing in the divergence field. Therefore, the divergence is inspected in Figure 4. The TRiSK energy conserving scheme cannot be recast in momentum advection form. Therefore, as expected, the TRiSK energy conserving scheme indeed features severe problems

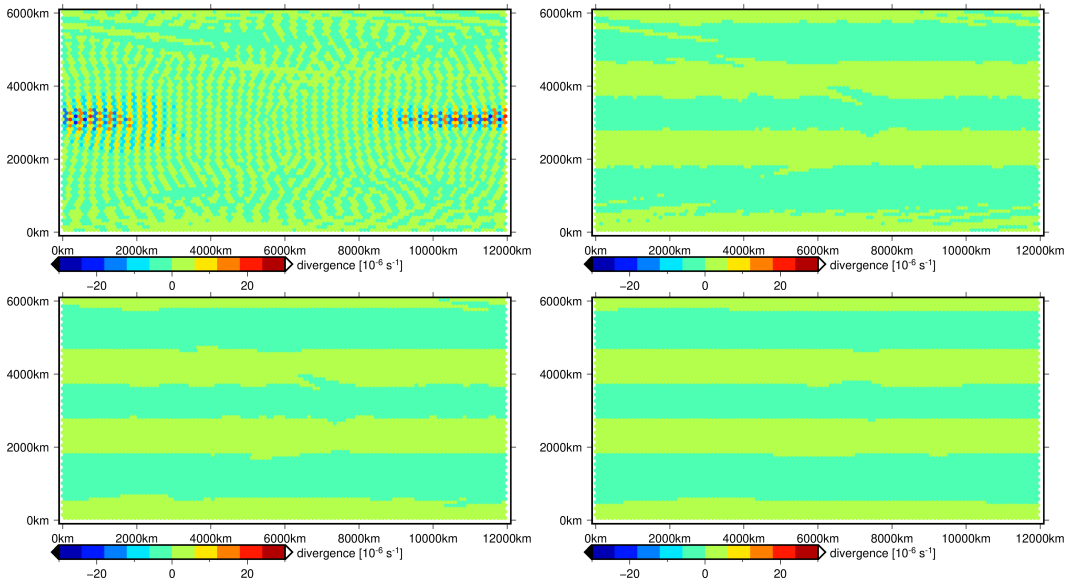

Figure 4. Divergence plotted on cells for the 0.1m depth flow. From top left to bottom right: TRSK energy conserving scheme, Gassmann (2018) scheme, Gassmann (2018) scheme with Smagorinsky diffusion, 3rd order upstream advection

in the divergence field. Also the vorticity field is corrupted in this case (not shown). In support of the argumentation given in Section 2.2 we conclude that the G18 scheme and derived schemes are not prone to the Hollingsworth instability.

4.2 Dry Atmosphere deformed mesh case

The ICON-IAP model (Gassmann, 2013, 2018) is run for studying the development of a dry baroclinic wave. Initial conditions are described in Gassmann (2019), results are shown for the state at day 9. Parameterizations are switched off, besides that one out of three runs employs Smagorinsky diffusion for the horizontal wind components, see G18. The grid resolution is 60 km, abbreviated with R2B6. 70 levels are used with about 400 m grid spacing in the vertical in the free troposphere. Three runs are now compared:

1. a run without diffusion
2. a run with Smagorinsky diffusion for the horizontal wind, where a background minimum shear is retained.
3. a run with the 3rd-order upstream add-on for momentum advection

The vorticity and horizontal divergence field are plotted on cell centers for three different heights in Figures 5 and 6. Colors are chosen for the runs with the 3rd-order upstream add-on, contours represent either the results without diffusion (left) or with Smagorinsky diffusion (right). The first observation is that the position of the fronts is almost identical in all cases. The vorticity isolines of runs 1 and 2 are very slightly lagged behind the those of run 3. This differs from the case when potential temperature advection schemes are compared in SG11, Figure 14. There it had been observed that 2nd-order advection of potential temperature lead to a slower developing cyclone compared to 3rd-order advection. This is not as much the case when comparing momentum advection schemes, and confirms the knowledge that the correct representation of baroclinity is decisive for a cyclone development. The second observation is that the vorticity field as well as the horizontal divergence field exhibit trailing wavy structures, hence typ-

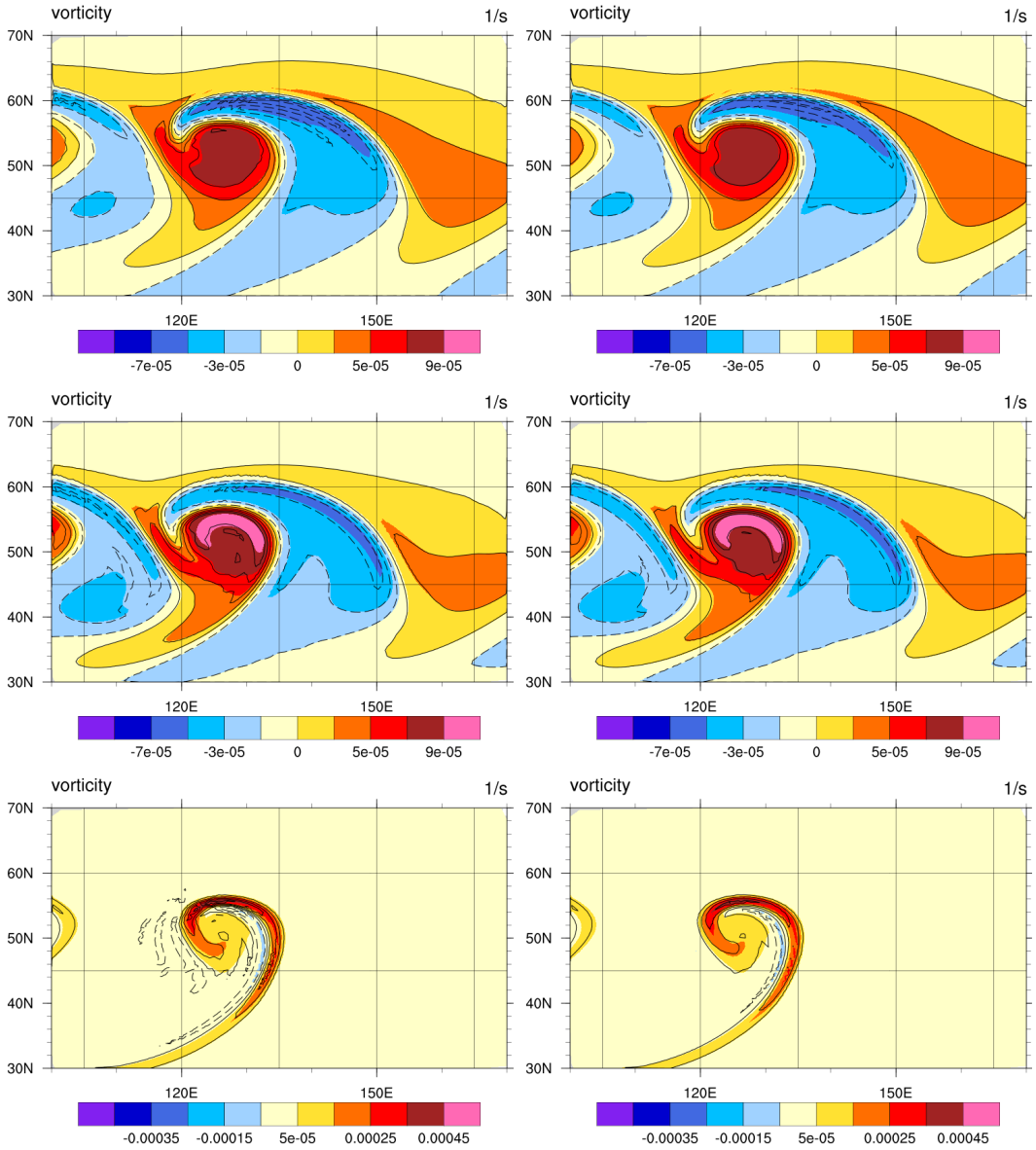

Figure 5. Relative vorticity fields comparing the run without diffusion (left, contoured) and Smagorinsky diffusion (right, contoured) with the 3rd order upstream scheme (colored). The contour intervals are the same as the color intervals. From top to bottom: level 45, 50 and 65 (6000 m, 4100 m and 400 m, respectively).

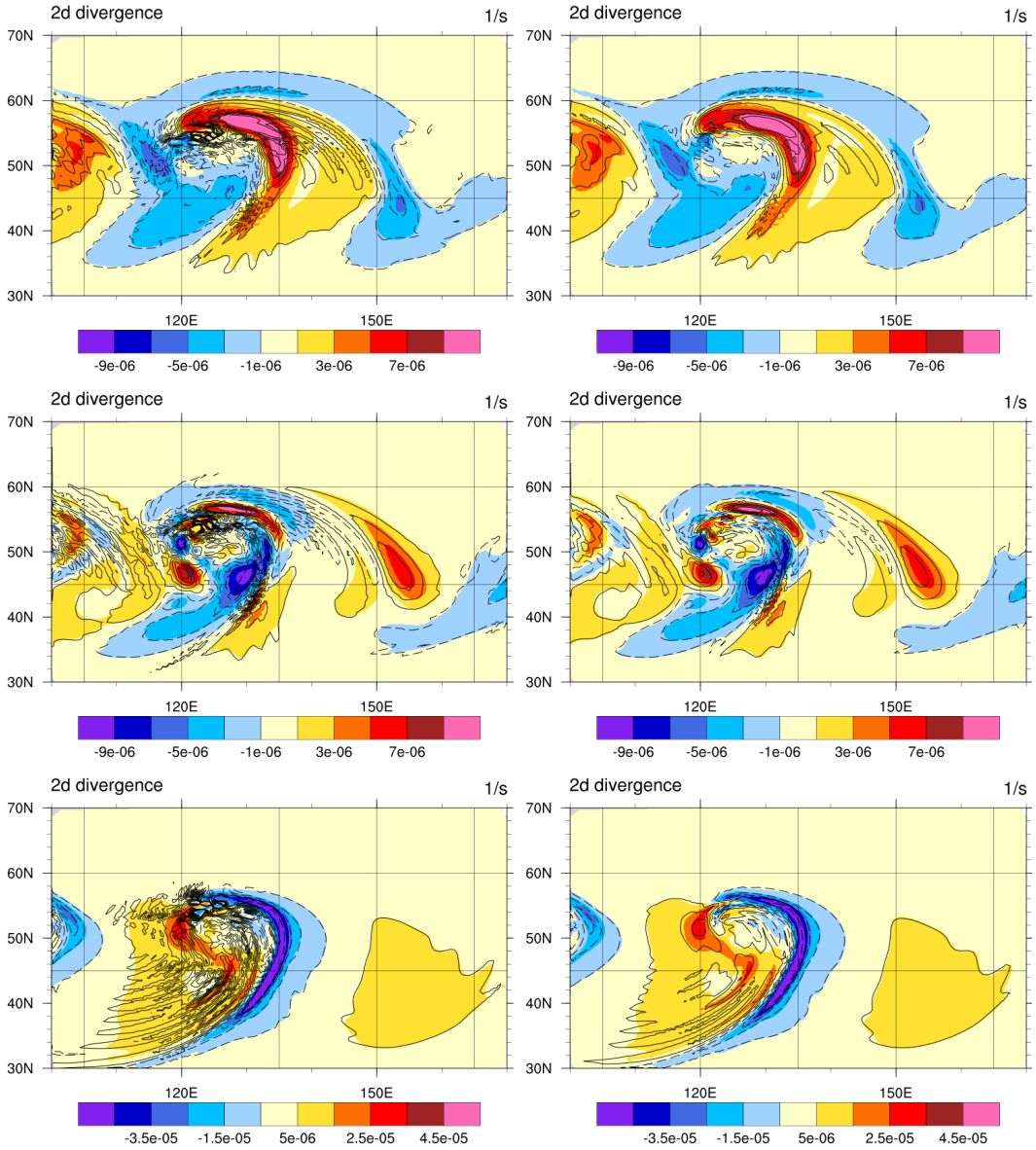

Figure 6. Horizontal divergence fields comparing the run without diffusion (left, contoured) and Smagorinsky diffusion (right, contoured) with the 3rd order upstream scheme (colored). The contour intervals are the same as the color intervals. From top to bottom: level 45, 50 and 65 (6000 m, 4100 m and 400 m, respectively).

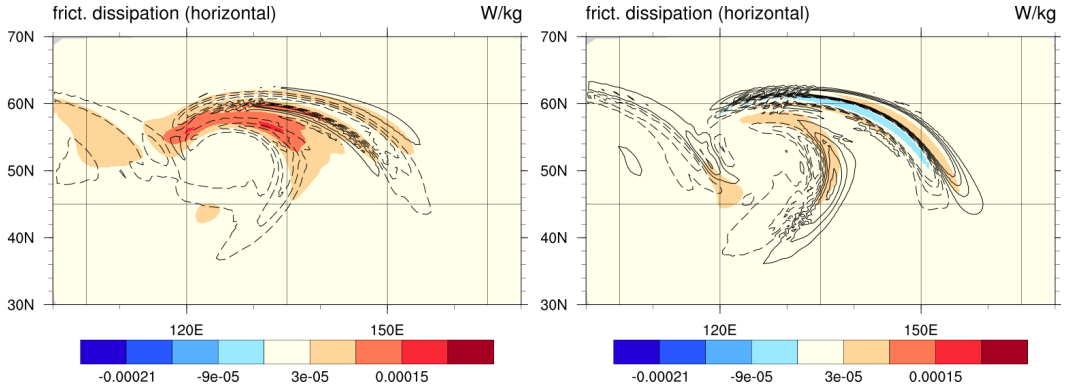

Figure 7. Properties of the dissipation for Smagorinsky diffusion (left) and the third order upstream add-on (right) at level 45. Dissipative heating (shear production) ε/ϱ in colors and frictional kinetic energy change $\dot{K}_{fric}$ in contours have the same interval spacing.

ical dispersion errors, behind the fronts. Their intensities are declining in sequence of the three runs. Those ripples do not severely show up in the vorticity field, but become dominant in case of the divergence field. Clearly, such structures form wave packets, and through general model dynamics they exhibit the characteristic dispersion properties of gravity waves, even though those ripples are predominantly not physically generated gravity waves. The third observation is that the second order scheme develops chaotic near grid scale structures in the horizontal divergence field, which are usually intended to be defeated by Smagorinsky diffusion. The run with the third-order add-on is far less affected by such grid-scale noise, only the horizontal divergence field at level 50 is slightly affected. Therefore, one can conclude that a model does not need further momentum diffusion, if the third-order advection scheme for momentum is used. Again, as in the SW-case, it should be noted that Smagorinsky diffusion is not able to defeat the trailing dispersion errors of even order advection schemes, because it is not constructed with any knowledge about the origin of those errors.

Interesting to observe are dissipation structures of the runs with Smagorinsky diffusion and the third order upstream add-on. Two aspects of momentum diffusion aspects are compared in the following. The first aspect is the direct effect on the tendency of the kinetic energy, which we call $\dot{K}_{fric}$ and the second aspect is the dissipative heating (or shear production), which represents the final conversion of dissipated kinetic energy into heat ε/ϱ. When mass weighted, both measures integrate finally to the same global values, which has been verified. But both measures have quite different local properties, see Figure 7. As expected, the Smagorinsky diffusion tends to erase the kinetic energy, only small areas at the flanks of the jet feature a slight kinetic energy increase. Dissipative heating is always positive and is located at the areas of gradients of kinetic energy loss. It is remarkable, that the amplitude of ε/ρ is smaller than the amplitudes in $\dot{K}_{fric}$ even though total integrals match. This can be explained by the fact that ε/ρ is a more smoothly spread measure. In contrast, the run with the upstream add-on features kinetic energy losses and gains with almost equal amplitudes. The gains of kinetic energy are always on the downstream side of the jet and the losses on the upstream side. This reflects the phase correction done by the third order scheme and explains the above described small phase differences in the location of the fronts. As known (Durran, 2010), 2nd-order advection has a relatively large phase error compared to higher order schemes. This is reflected by a numerically reproduced slower speed of the initial front and even slower trailing spikes (Durran (2010), e. g. Fig. 3.7). The total amount of kinetic energy loss is quite small. The dissipated energy ε/ϱ is more locally converted into heat in comparison to

the Smagorinsky model. It features negative and positive values with a positive global mean. This highlights that 3rd-order advection has diffusive and antidiffusive parts, which result in dissipative and antidissipative properties. Generally speaking, the antidissipative property could be interpreted as energy backscatter in a physical sense, but it is a numerical necessity to avoid unphysical trailing ripples.

The reason for the very different properties of runs 2 and 3 with regard to dissipation lays in the fact that both schemes work out of two different perspectives. The Smagorinsky model assumes that it represents physics and disregards that the field on which it acts has already a numerical errors, but it correctly assumes that it must dissipate energy where the flow deformation is high. The decisive deformation in the Smagorinsky model is a property of the horizontal 2d-plane, whereas the character of the 3rd-order upstream add-on inspects the flow in dependence on the upstream 1d-direction.

5 Conclusion

This contribution demonstrates how the 3rd-order upstream scalar advection scheme on Voronoi C-grids of SG11 can be generalized to be applicable for horizontal momentum advection. As outlined in Section 3, this is not a trivial task, because the advection velocity, the required directional Laplacian of a specific wind component, and the upstream direction have to be calculated on the deformed mesh. The prerequisite for the applicability of this generalization is that the vector-invariant form of momentum advection should be as equivalent to the second order momentum advection form as possible. It has been shown that a term, which signifies a tiny deviation from this idealization, does not lead to the danger of the Hollingsworth instability. Also, the remaining checkerboard pattern of the vorticity on triangles is irrelevant because only vorticities on edges enter the computation. Hence there is no need to fight the checkerboard on triangles explicitly via a further diffusive mechanism.

The comparison of regular mesh shallow water and deformed mesh dry atmosphere runs with several configurations reveals that numerically generated dispersion errors of 2nd-order schemes with or without Smagorinsky diffusion may trigger gravity waves and vorticity disturbances such that the flow far away from the source might be affected. Then, it will be impossible to identify the respective structures as being a result of a numerical error. Smagorinsky diffusion damps the amplitudes of those waves but does not prohibit their formation. This accomplishes only the 3rd-order add-on.

The Smagorinsky diffusion and its guaranteed locally positive definite dissipation rate is an idealization which requires implicitly a numerical flow without dispersion errors. So, it may be applicable in other contexts than the finite-volume C-grid environments, for instance in spectral models or as a turbulence parameterization which is applied in a model with already higher-order upstream momentum advection in the dynamical core. But nevertheless such a dynamical core would feature some antidiffusion because of the usage of the upstream advection scheme.

The 3rd-order upstream scheme avoids not only trailing dispersive ripples, but also shifts the position of the fronts of the baroclinic wave slightly to the east. This effect is expectable, but negligible.

The formulation of the momentum advection might be tuned by varying the factor 1/12 in (28) to become a bit larger. Such, the diffusion would be slightly enhanced and Fromm's scheme would result if this factor would be set to 1/8. Future research could also aim at a blending between Smagorinsky diffusion and the upstream add-on.

With the present contribution, numerical schemes on the hexagonal C-grid have reached full equivalence to comparable schemes on the quadrilateral C-grid. We can say

that a development line starting with the kick-off contribution of Thuburn (2008) is about to have reached its end.

Appendix A Reconstruction rules

Two different reconstruction rules are needed for our purposes:

1. For velocity vectors and their gradients, namely the advective velocity in the center of a hexagon and the gradients which appear in the deformations E^1, F_2^1, F_3^1. (see equations (21)-(23))
2. For the gradients of the directional Laplacians in the centers of the hexagons and rhombi, respectively.

A1 Velocity vectors and their gradients

For the sake consistency with previous work, Appendix A of Gassmann (2018) is here recapitulated.

The Taylor expansion at the rhombus center r for the velocity is

$$\mathbf{v} = \mathbf{e}_x(u_r + \frac{\partial u}{\partial y}\, dx_r \frac{y-y_r}{dx_r}) + \mathbf{e}_y(v_r + \frac{\partial v}{\partial x}\, dx_r \frac{x-x_r}{dx_r}), \tag{A1}$$

where $\mathbf{e}_x$ and $\mathbf{e}_y$ are the base vectors in the required coordinate system of a target edge; $\mathbf{e}_x$ is the unit normal vector on the edge, and $\mathbf{e}_y$ is the righthanded tangential vector on this target edge. The Taylor expansion omits the terms with the derivatives $\partial_x u$ and $\partial_y v$. This omission degrades the accuracy of the gradient reconstruction if the mesh is deformed. However, the stencil for the gradient reconstruction remains the same as for the vorticity which is combined with this reconstruction. Peixoto (2016) mentioned a similar degradation of the accuracy below 2nd order if vorticity or divergence are computed with the discrete Stokes or Gauss theorems on deformed meshes. This drawback is inherent to all C-grid disretizations on geodesic grids.

The unknown variables in (A1) are $\mathbf{c} = \{u_r, v_r, \widetilde{\partial_y u} = \partial_y u\ dx_r, \widetilde{\partial_x v} = \partial_x v\ dx_r\}$. The weighting of the last two unknowns with a reference length dx_r allows the matrix to contain values of the same order of magnitude. The distances $y-y_r$ and $x-x_r$ are evaluated as great circle distances on the sphere. Each normal wind component on a cell edge is likewise a tangential wind component at a rhombus edge, $u_e = \mathbf{N_e} \cdot \mathbf{v}$, where $\mathbf{N_e}$ is the local unit normal vector at an edge. A set of wind components on rhombi are combined to the vector $\mathbf{u} = \{u_e\}$. The problem to solve is now

$$\mathbf{u} = \left\{ \mathbf{N_e}\cdot\mathbf{e}_x \quad \mathbf{N_e}\cdot\mathbf{e}_y \quad \mathbf{N_e}\cdot\mathbf{e}_x \tfrac{dy_i}{dx_r} \quad \mathbf{N_e}\cdot\mathbf{e}_y \tfrac{dx_i}{dx_r} \right\} \cdot \begin{pmatrix} u_r \\ v_r \\ \widetilde{\partial_y u} \\ \widetilde{\partial_x v} \end{pmatrix}. \tag{A2}$$

This is a matrix equation

$$\mathbf{u} = \mathbf{M} \cdot \mathbf{c}. \tag{A3}$$

The solution of the equation is found by application of a QR decomposition. The solution vector is thus

$$\mathbf{c} = \mathbf{R}^{-1} \cdot \mathbf{Q}^T \cdot \mathbf{u}. \tag{A4}$$

The required meridional velocity gradient is $\partial_y u = \widetilde{\partial_y u}/dx_r$.

A similar method is used for the least squares reconstruction of the velocity gradient for a hexagon. Then, the velocity is represented as

$$\mathbf{v} = \mathbf{e}_x(u_c + \frac{\partial u}{\partial x}\, dx_r \frac{x-x_c}{dx_r}) + \mathbf{e}_y(v_c + \frac{\partial v}{\partial y}\, dx_r \frac{y-y_c}{dx_r}). \tag{A5}$$

Here, the expansion terms with the derivatives $\partial_x v$ and $\partial_y u$ are omitted. The vector $\mathbf{u}$ contains the normal wind components at the edges of a hexagon. Then, matrix $\mathbf{M}$ is no longer a square matrix, but there are more knowns than unknowns and a similar solution as (A4) gets a least square interpretation.

A2 Reconstruction of the directional Laplacians

The reconstruction of the directional Laplacians requires a different procedure than above, because we are not dealing with velocities. Therefore, the relations

$$\begin{aligned} \partial_{xx}u\ \mathbf{e}_x\mathbf{e}_x\mathbf{e}_x &= \partial_x(\partial_x(u\mathbf{e}_x)\mathbf{e}_x)\mathbf{e}_x && \text{(A6)}\\ \partial_{yy}v\ \mathbf{e}_y\mathbf{e}_y\mathbf{e}_y &= \partial_y(\partial_y(v\mathbf{e}_y)\mathbf{e}_y)\mathbf{e}_y && \text{(A7)}\\ \partial_{nn}u_e\ \mathbf{N}_e\mathbf{N}_e\mathbf{N}_e &= \partial_n(\partial_n(u_e\mathbf{N}_e)\mathbf{N}_e)\mathbf{N}_e && \text{(A8)} \end{aligned}$$

have to be taken into acount. Here, a derivative in normal direction $\mathbf{N}_e$ is indicated by n. In order to reconstruct the gradient of the directional Laplacian on the cells (hexagons or pentagons), only the directional Laplacians $\partial_{nn}u_e$ at every edge are necessary. A Taylor expansion of the directional Laplacians in the coordinate system of the target edge around the cell's center of a hexagon reads thus

$$\begin{bmatrix} \delta_{11}u_{e1}\\ \delta_{22}u_{e2}\\ \delta_{33}u_{e3}\\ \delta_{44}u_{e4}\\ \delta_{55}u_{e5}\\ \delta_{66}u_{e6} \end{bmatrix} = \begin{bmatrix} (\mathbf{e}_x\cdot\mathbf{N}_1)^3 & (\mathbf{e}_y\cdot\mathbf{N}_1)^3 & (\mathbf{e}_x\cdot\mathbf{N}_1)^3\Delta x_1 & (\mathbf{e}_y\cdot\mathbf{N}_1)^3\Delta y_1\\ (\mathbf{e}_x\cdot\mathbf{N}_2)^3 & (\mathbf{e}_y\cdot\mathbf{N}_2)^3 & (\mathbf{e}_x\cdot\mathbf{N}_2)^3\Delta x_2 & (\mathbf{e}_y\cdot\mathbf{N}_2)^3\Delta y_2\\ (\mathbf{e}_x\cdot\mathbf{N}_3)^3 & (\mathbf{e}_y\cdot\mathbf{N}_3)^3 & (\mathbf{e}_x\cdot\mathbf{N}_3)^3\Delta x_3 & (\mathbf{e}_y\cdot\mathbf{N}_3)^3\Delta y_3\\ (\mathbf{e}_x\cdot\mathbf{N}_4)^3 & (\mathbf{e}_y\cdot\mathbf{N}_4)^3 & (\mathbf{e}_x\cdot\mathbf{N}_4)^3\Delta x_4 & (\mathbf{e}_y\cdot\mathbf{N}_4)^3\Delta y_4\\ (\mathbf{e}_x\cdot\mathbf{N}_5)^3 & (\mathbf{e}_y\cdot\mathbf{N}_5)^3 & (\mathbf{e}_x\cdot\mathbf{N}_5)^3\Delta x_5 & (\mathbf{e}_y\cdot\mathbf{N}_5)^3\Delta y_5\\ (\mathbf{e}_x\cdot\mathbf{N}_6)^3 & (\mathbf{e}_y\cdot\mathbf{N}_6)^3 & (\mathbf{e}_x\cdot\mathbf{N}_6)^3\Delta x_6 & (\mathbf{e}_y\cdot\mathbf{N}_6)^3\Delta y_6 \end{bmatrix} \cdot \begin{bmatrix} \partial_{xx}u\\ \partial_{yy}v\\ \partial_x(\partial_{xx}u)\\ \partial_y(\partial_{yy}v) \end{bmatrix} \qquad \text{(A9)}$$

The non-dimensional Laplacians on the left are now to be read as that all stored local $\delta_{11}u_{1e}$-values are included therein, see last remark in subsection 3.3. The distances from the cells to the edges Δx_i nd Δy_i are expressed with the help of the half dual edge length d_i

$$(\mathbf{e}_x\cdot\mathbf{N}_i)^3\Delta x_i = (\mathbf{e}_x\cdot\mathbf{N}_i)^4\frac{d_i}{2}\gamma_c^{out,i} \qquad (\mathbf{e}_y\cdot\mathbf{N}_i)^3\Delta y_i = (\mathbf{e}_y\cdot\mathbf{N}_i)^4\frac{d_i}{2}\gamma_c^{out,i} \qquad \text{(A10)}$$

In practice, only the directional gradient reconstruction $\partial_x(\partial_{xx}u)$ is necessary for equation (29).

For the rhombi we had computed the directional Laplacians as if they were taken as a tangential derivative, and not directly in 2- or 3-direction, even though we assign them as $\delta_{22}u_e$ and $\delta_{33}u_e$. But because we take these tangential derivatives of the tangential gradients twice, once from upper left to lower right, and once between lower left and upper right, we have to do the following computations also two times in order to catch both types of directions. In the case of rhombi, the tangential Laplacians of a normal velocity are the relevant measures

$$\begin{aligned} \partial_{yy}u\ \mathbf{e}_x\mathbf{e}_y\mathbf{e}_y &= \partial_y(\partial_y(u\mathbf{e}_x)\mathbf{e}_y)\mathbf{e}_y && \text{(A11)}\\ \partial_{xx}v\ \mathbf{e}_y\mathbf{e}_x\mathbf{e}_x &= \partial_x(\partial_x(v\mathbf{e}_y)\mathbf{e}_x)\mathbf{e}_x && \text{(A12)}\\ \partial_{tt}u_e\ \mathbf{N}_e\mathbf{T}_e\mathbf{T}_e &= \partial_t(\partial_t(u_e\mathbf{N}_e)\mathbf{T}_e)\mathbf{T}_e && \text{(A13)} \end{aligned}$$

Now, relevant projections are $\eta_i = \mathbf{e}_y\cdot\mathbf{T}_i$, $\beta_i = \mathbf{e}_x\cdot\mathbf{T}_i$, $\gamma_i = \mathbf{e}_y\cdot\mathbf{N}_i$, $\alpha_i = \mathbf{e}_x\cdot\mathbf{N}_i$. With them, the Taylor expansion for a directional Laplacian in the center of a rhombus reads

$$\begin{bmatrix} \delta_{11}^{tt}u_{e1}\\ \delta_{22}^{tt}u_{e2}\\ \delta_{33}^{tt}u_{e3}\\ \delta_{44}^{tt}u_{e4} \end{bmatrix} = \begin{bmatrix} \eta_1^2\alpha_1 & \beta_1^2\gamma_1 & \eta_1^2\alpha_1\Delta y_1 & \beta_1^2\gamma_1\Delta x_1\\ \eta_2^2\alpha_2 & \beta_2^2\gamma_2 & \eta_2^2\alpha_2\Delta y_2 & \beta_2^2\gamma_2\Delta x_2\\ \eta_3^2\alpha_3 & \beta_3^2\gamma_3 & \eta_3^2\alpha_3\Delta y_3 & \beta_3^2\gamma_3\Delta x_3\\ \eta_4^2\alpha_4 & \beta_4^2\gamma_4 & \eta_4^2\alpha_2\Delta y_4 & \beta_4^2\gamma_2\Delta x_4 \end{bmatrix} \cdot \begin{bmatrix} \partial_{yy}u\\ \partial_{xx}v\\ \partial_y(\partial_{yy}u)\\ \partial_x(\partial_{xx}v) \end{bmatrix} \qquad \text{(A14)}$$

The superscript tt signifies that we deal with tangential derivatives. The non-dimensional Laplacians on the left are now to be read as that all stored local $\delta_{22}u_e$-values or $\delta_{33}u_e$-values, respectively, are taken, see last remark in subsection 3.3. Finally, we need for our purposes only the tangential directional gradient $\partial_y(\partial_{yy}u)$. We distinguish between (i) the tangential gradients which are representing the 3-directions going from upper right to lower left, where only the 3-directed directional Laplacians form the left hand side, and (ii) the tangential gradients which are representing the 2-direction going from lower right to upper left, where only the 2-directed directional Laplacians form the left hand side in the Taylor expansion. The distances between the rhombus centers and the edges Δx_i and Δy_i are directly obtained as great circle arcs on the sphere.

Appendix B Open Research

The shallow water code, relevants parts of the source code of the ICON-IAP model, and the raw data which are plotted in the figures are available from a zenodo repository (Gassmann, 2022).

Acknowledgments

I sincerely thank Sergey Danilov (AWI Bremerhaven) for enduring encouragement and critical accompanying feedback at all stages of the work during the last year. This paper is a contribution to the project M3 "Toward consistent momentum closures" of the Collaborative Research Centre TRR 181 "Energy Transfers in Atmosphere and Ocean" funded by the Deutsche Forschungsgemeinschaft (DFG, German Research Foundation) - Projektnummer 274762653. I thank IAP Kühlungsborn for providing computing facilities.

References

Dubos, T., Dubey, S., Tort, M., Mittal, R., Meurdesoif, Y., & Hourdin, F. (2015). Dynamico-1.0, an icosahedral hydrostatic dynamical core designed for consistency and versatility. *Geosci. Model Dev.*, *8*(10), 3131–3150. doi: 10.5194/gmd-8-3131-2015

Durran, D. (2010). *Numerical methods for fluid dynamics* (2nd ed.). Springer New York, NY. doi: 0.1007/978-1-4419-6412-0

Gassmann, A. (2011). Inspection of hexagonal and triangular C-grid discretizations of the shallow water equations. *J. Comput. Phys.*, *230*(7), 2706-2721. doi: 10.1016/j.jcp.2011.01.014

Gassmann, A. (2013). A global hexagonal C-grid non-hydrostatic dynamical core (ICON-IAP) designed for energetic consistency. *Quarterly Journal of the Royal Meteorological Society*, *139*(670), 152-175. doi: 10.1002/qj.1960

Gassmann, A. (2018). Discretization of generalized Coriolis and friction terms on the deformed hexagonal C-grid. *Quart. J. Roy. Meteor. Soc.*, *144*(716), 2038-2053. doi: 10.1002/qj.3294

Gassmann, A. (2019). Analysis of large-scale dynamics and gravity waves under shedding of inactive flow components. *Mon. Wea. Rev.*, *147*(8), 2861 - 2876. doi: 10.1175/MWR-D-18-0349.1

Gassmann, A. (2021). Inherent dissipation of upwind-biased potential temperature advection and its feedback on model dynamics. *J. Adv. Model. Earth Syst.*, *13*(3), e2020MS002384. doi: 10.1029/2020MS002384

Gassmann, A. (2022). *Third-order momentum advection on the1 quasi-hexagonal C-grid on the sphere: Data and source code* [dataset]. zenodo.org. Retrieved from `https://zenodo.org/record/7048652#.YxUDe9JBxhF` doi: 10.5281/zenodo.7048652

Herzfeld, M., Engwirda, D., & Rizwi, F. (2020). A coastal unstructured model us-

ing voronoi meshes and c-grid staggering. *Ocean Modell.*, *148*, 101599. doi: 10.1016/j.ocemod.2020.101599

Hollingsworth, A., Kållberg, P., Renner, V., & Burridge, D. M. (1983). An internal symmetric computational instability. *Quart. J. Roy. Meteor. Soc.*, *109*(460), 417-428. doi: 10.1002/qj.49710946012

Klemp, J. B. (2017). Damping characteristics of horizontal Laplacian diffusion filters. *Mon. Wea. Rev.*, *145*(11), 4365 - 4379. doi: 10.1175/MWR-D-17-0015.1

Korn, P. (2017). Formulation of an unstructured grid model for global ocean dynamics. *J. Comput. Phys.*, *339*, 525-552. doi: 10.1016/j.jcp.2017.03.009

Kühnlein, C., Deconinck, W., Klein, R., Malardel, S., Piotrowski, Z. P., Smolarkiewicz, P. K., ... Wedi, N. P. (2019). FVM 1.0: a nonhydrostatic finite-volume dynamical core for the IFS. *Geosci. Model Dev.*, *12*(2), 651–676. doi: 10.5194/gmd-12-651-2019

Miura, H., & Skamarock, W. C. (2013). An upwind-biased transport scheme using a quadratic reconstruction on spherical icosahedral grids. *Mon. Wea. Rev.*, *141*(2), 832 - 847. doi: 10.1175/MWR-D-11-00355.1

Peixoto, P. S. (2016). Accuracy analysis of mimetic finite volume operators on geodesic grids and a consistent alternative. *J. Comput. Phys.*, *310*, 127-160. doi: 10.1016/j.jcp.2015.12.058

Randall, D. A. (1994). Geostrophic adjustment and the finite-difference shallow-water equations. *Mon. Wea. Rev.*, *122*(6), 1371 - 1377. doi: 10.1175/1520-0493(1994)122⟨1371:GAATFD⟩2.0.CO;2

Ringler, T., Petersen, M., Higdon, R. L., Jacobsen, D., Jones, P. W., & Maltrud, M. (2013). A multi-resolution approach to global ocean modeling. *Ocean Modell.*, *69*, 211-232. doi: 10.1016/j.ocemod.2013.04.010

Ringler, T., Thuburn, J., Klemp, J., & Skamarock, W. (2010). A unified approach to energy conservation and potential vorticity dynamics for arbitrarily-structured C-grids. *J. Comput. Phys.*, *229*(9), 3065-3090. doi: 10.1016/j.jcp.2009.12.007

Sadourny, R. (1975). The dynamics of finite-difference models of the shallow-water equations. *J. Atmos. Sci.*, *32*(4), 680 - 689. doi: 10.1175/1520-0469(1975)032\⟨0680:TDOFDM\⟩2.0.CO\;2

Skamarock, W. C., & Gassmann, A. (2011). Conservative transport schemes for spherical geodesic grids: High-order flux operators for ODE-based time integration. *Mon. Wea. Rev.*, *139*(9), 2962 - 2975. doi: 10.1175/MWR-D-10-05056.1

Skamarock, W. C., Klemp, J. B., Duda, M. G., Fowler, L. D., Park, S.-H., & Ringler, T. D. (2012). A multiscale nonhydrostatic atmospheric model using centroidal Voronoi tesselations and C-grid staggering. *Mon. Wea. Rev.*, *140*(9), 3090 - 3105. doi: 10.1175/MWR-D-11-00215.1

Smagorinsky, J. (1993). Large eddy simulation of complex engineering and geophysical flows. In B. Galperin & S. A. Orszag (Eds.), (p. 3-36). Cambridge University Press.

Soontiens, N., & Allen, S. E. (2017). Modelling sensitivities to mixing and advection in a sill-basin estuarine system. *Ocean Modell.*, *112*, 17-32. doi: 10.1016/j.ocemod.2017.02.008

Subich, C. J. (2018). Higher-order finite volume differential operators with selective upwinding on the icosahedral spherical grid. *J. Comput. Phys.*, *368*, 21-46. doi: 10.1016/j.jcp.2018.04.053

Thuburn, J. (2008). Numerical wave propagation on the hexagonal C-grid. *J. Comput. Phys.*, *227*(11), 5836-5858. doi: 10.1016/j.jcp.2008.02.010

Thuburn, J., Ringler, T., Skamarock, W., & Klemp, J. (2009). Numerical representation of geostrophic modes on arbitrarily structured C-grids. *J. Comput. Phys*, *228*(22), 8321-8335. doi: 10.1016/j.jcp.2009.08.006

Weller, H. (2012). Controlling the computational modes of the arbitrarily structured C-grid. *Mon. Wea. Rev.*, *140*(10), 3220 - 3234. doi: 10.1175/MWR-D-11-00221

.1

Zhang, Y., Li, J., Yu, R., Zhang, S., Liu, Z., Huang, J., & Zhou, Y. (2019). A layer-averaged nonhydrostatic dynamical framework on an unstructured mesh for global and regional atmospheric modeling: Model description, baseline evaluation, and sensitivity exploration. *J. Adv. Model. Earth Syst.*, *11*(6), 1685-1714. doi: 10.1029/2018MS001539

Zängl, G., Reinert, D., Ripodas, P., & Baldauf, M. (2015). The ICON (ICOsahedral Non-hydrostatic) modelling framework of DWD and MPI-M: Description of the non-hydrostatic dynamical core. *Quart. J. Roy. Meteor. Soc.*, *141*(687), 563-579. doi: 10.1002/qj.2378